



Cite this: *Nanoscale Adv.*, 2024, **6**, 1781

## Construction of a $\text{BiVO}_4/\text{V}_\text{S}-\text{MoS}_2$ S-scheme heterojunction for efficient photocatalytic nitrogen fixation†

Han-Ying Luo,<sup>‡,a</sup> Zhao-Lei Liu,<sup>‡,a</sup> Meng-Ran Zhang,<sup>a</sup> Yan-Fei Mu,<sup>‡,b</sup> and Min Zhang,<sup>ID, \*a</sup>

Photocatalytic nitrogen ( $\text{N}_2$ ) reduction to ammonia ( $\text{NH}_3$ ), adopting  $\text{H}_2\text{O}$  as the electron source, suffers from low efficiency owing to the sluggish kinetics of  $\text{N}_2$  reduction and the requirement of a substantial thermodynamic driving force. Herein, we present a straightforward approach for the construction of an S-scheme heterojunction of  $\text{BiVO}_4/\text{V}_\text{S}-\text{MoS}_2$  to successfully achieve photocatalytic  $\text{N}_2$  fixation, which is manufactured by coupling an  $\text{N}_2$ -activation component ( $\text{V}_\text{S}-\text{MoS}_2$  nanosheet) and water-oxidation module ( $\text{BiVO}_4$  nanocrystal) through electrostatic self-assembly. The  $\text{V}_\text{S}-\text{MoS}_2$  nanosheet, enriched with sulfur vacancies, plays a pivotal role in facilitating  $\text{N}_2$  adsorption and activation. Additionally, the construction of the S-scheme heterojunction enhances the driving force for water oxidation and improves charge separation. Under simulated sunlight irradiation ( $100 \text{ mW cm}^{-2}$ ),  $\text{BiVO}_4/\text{V}_\text{S}-\text{MoS}_2$  exhibits efficient photocatalytic  $\text{N}_2$  reduction activity with  $\text{H}_2\text{O}$  as the proton source, yielding  $\text{NH}_3$  at a rate of  $132.8 \mu\text{mol g}^{-1} \text{ h}^{-1}$ , nearly 7 times higher than that of pure  $\text{V}_\text{S}-\text{MoS}_2$ . This study serves as a noteworthy example of efficient  $\text{N}_2$  reduction to  $\text{NH}_3$  under mild conditions.

Received 8th December 2023  
Accepted 19th February 2024

DOI: 10.1039/d3na01091k  
[rsc.li/nanoscale-advances](http://rsc.li/nanoscale-advances)

## 1. Introduction

Ammonia ( $\text{NH}_3$ ) serves as both a promising energy storage intermediary and an essential raw material affecting agricultural and industrial production.<sup>1,2</sup> However, given the molecular inertness of  $\text{N}_2$  (dissociation energy of  $945 \text{ kJ mol}^{-1}$ ), the current industrial synthesis of  $\text{NH}_3$  predominantly relies on the Haber–Bosch process.<sup>3,4</sup> This traditional method requires high temperature and pressure ( $300\text{--}550 \text{ }^\circ\text{C}$  and  $15\text{--}25 \text{ MPa}$ ), resulting in significant investment costs and high energy consumption.<sup>5,6</sup> Therefore, the pursuit of synthetic processes under mild conditions has become a paramount objective. Photocatalytic  $\text{N}_2$  fixation, employing semiconductor photocatalysts that harness sunlight as the energy source while utilizing  $\text{N}_2$  and  $\text{H}_2\text{O}$  as reactants, stands out as a sustainable approach for  $\text{NH}_3$  production.<sup>7–10</sup> Nonetheless, because of the poor  $\text{N}_2$  adsorption–activation and carrier separation in

semiconductor photocatalysts, achieving efficient photocatalytic conversion of  $\text{N}_2$  to  $\text{NH}_3$  remains a scientific challenge.<sup>11–13</sup>

Efficient  $\text{N}_2$  adsorption–activation and good light absorption of photocatalysts are the fundamental prerequisites for realizing the efficient photoreduction of  $\text{N}_2$  to produce  $\text{NH}_3$ .<sup>14</sup> Consequently, the initial step involves the selection of potential semiconductor materials to reasonably design photocatalysts with suitable energy levels for  $\text{N}_2$  reduction and favorable properties for  $\text{N}_2$  adsorption–activation.<sup>15–17</sup> Schrauzer and co-workers conducted the pioneering systematic investigation into the photocatalytic  $\text{NH}_3$  synthesis using  $\text{TiO}_2$ -based materials.<sup>18</sup> In recent years, numerous studies have explored traditional metal oxides, carbonaceous materials, and layered double hydroxide semiconductors as photocatalysts for  $\text{N}_2$  photofixation.<sup>19–22</sup> However, these semiconductor materials often exhibit wide band gaps and narrow spectral absorption characteristics, which are not conducive for efficient photon utilization in photocatalytic reactions. Inspired by the MoFe-cofactor in natural nitrogenase, molybdenum disulfide ( $\text{MoS}_2$ ) has garnered significant attention in the field of  $\text{N}_2$  fixation due to its structural resemblance to nitrogenase with a Mo–S configuration.<sup>23,24</sup> As a two-dimensional direct bandgap semiconductor material,  $\text{MoS}_2$  not only possesses good photon capture ability but also can be used as a carrier to construct composite catalysts to achieve more efficient catalytic conversion. Nonetheless,  $\text{MoS}_2$  exhibits poor activity in photocatalytic  $\text{N}_2$  reduction systems using water as the electron source due to

<sup>a</sup>MOE International Joint Laboratory of Materials Microstructure, Institute for New Energy Materials and Low Carbon Technologies, School of Materials Science and Engineering, School of Chemistry and Chemical Engineering, Tianjin University of Technology, Tianjin 300384, China. E-mail: zm2016@mail.tjut.edu.cn

<sup>b</sup>School of Chemistry and Chemical Engineering, Yangzhou University, Yangzhou, Jiangsu 225009, China. E-mail: 007916@yzu.edu.cn

† Electronic supplementary information (ESI) available: Materials, characterization approaches, and some supporting data. See DOI: <https://doi.org/10.1039/d3na01091k>

‡ Han-Ying Luo and Zhao-Lei Liu contributed equally to this work.



its lack of water oxidation capacity.<sup>25</sup> In addition, akin to other semiconductor photocatalysts, its weak photogenerated carrier separation ability also hinders the progress of photocatalytic N<sub>2</sub> reduction.<sup>26,27</sup> To improve the photocatalytic activity of semiconductor photocatalysts, extensive research efforts have focused on bolstering charge separation through the construction of p-n, II-type, and S-scheme heterojunctions.<sup>28-31</sup> Mimicking natural photosynthesis, the S-scheme charge transfer system has received special attention, which can simultaneously facilitate spatial carrier separation and improve redox ability.<sup>32,33</sup> Additionally, monoclinic BiVO<sub>4</sub> as a “star” material has a broad range of visible light utilization and excellent photoelectric stability, and has been widely used in the study of photoanodic water oxidation.<sup>34</sup> Based on this, BiVO<sub>4</sub> has potential to serve as a water oxidation unit for MoS<sub>2</sub> to construct heterojunctions, further enhancing the efficiency of photocatalytic N<sub>2</sub> fixation.

Herein, we present an innovative S-scheme heterojunction prepared by coupling sulfur vacancy enriched MoS<sub>2</sub> nanosheets (V<sub>S</sub>-MoS<sub>2</sub>) with BiVO<sub>4</sub> nanocrystals through electrostatic self-assembly for photocatalytic N<sub>2</sub> reduction. Under simulated sunlight irradiation (100 mW cm<sup>-2</sup>), BiVO<sub>4</sub>/V<sub>S</sub>-MoS<sub>2</sub> exhibits efficient photocatalytic N<sub>2</sub> reduction activity, with a NH<sub>3</sub> yield of 132.8 μmol g<sup>-1</sup> h<sup>-1</sup>, nearly 7 times that of pure V<sub>S</sub>-MoS<sub>2</sub> (20 μmol g<sup>-1</sup> h<sup>-1</sup>). In addition, the experimental results from *in situ* X-ray photoelectron spectroscopy and electron spin resonance spectroscopy verify the presence of sulfur-rich vacancies on the surface of V<sub>S</sub>-MoS<sub>2</sub> nanosheets and the successful formation of an S-scheme heterojunction, which are conducive to the improvement of N<sub>2</sub> adsorption–activation and driving force of water oxidation as well as charge separation. The mechanism of the N<sub>2</sub> reduction reaction is speculated using *in situ* diffuse reflectance infrared Fourier transform spectroscopy.

## 2. Experimental

### 2.1. Sample preparation

**2.1.1. Preparation of V<sub>S</sub>-MoS<sub>2</sub> nanosheets.** Na<sub>2</sub>MoO<sub>4</sub>·2H<sub>2</sub>O (243 mg) and CH<sub>4</sub>N<sub>2</sub>S (304 mg) were dissolved in ultrapure water (35 mL). After 30 min of stirring, the mixture was transferred to a 50 mL Teflon autoclave and heated at 180 °C for 48 h. Subsequently, the products were washed 3 times with a 0.1 M HCl solution to eliminate any residual nitrogen in the sample. The V<sub>S</sub>-MoS<sub>2</sub> nanosheet powder can be obtained after vacuum drying at 60 °C for 12 h.

**2.1.2. Preparation of BiVO<sub>4</sub> nanocrystals.** In a three-neck flask, a mixture containing 484 mg of Bi(NO<sub>3</sub>)<sub>3</sub>·5H<sub>2</sub>O, 20 mL of octadecene, 3 mL of oleylamine, and 3 mL of oleic acid was heated to 170 °C until it became transparent, and then stored at 100 °C. NaVO<sub>3</sub> (242 mg) was dissolved in ultrapure water (20 mL) at 100 °C, and added to the above three-neck flask. The resulting mixture was poured into ethanol to induce precipitation. Afterward, it was subjected to three rounds of washing with a hexane and ethanol mixture, followed by vacuum drying at 60 °C for 12 h to obtain a yellow-green BiVO<sub>4</sub> nanocrystal. For further purification, the obtained BiVO<sub>4</sub> quantum dots (20 mg) were dispersed in a solution comprising 10 mL of isopropanol

and 1 mL of KI in DMSO (0.1 M). Ultrasonic treatment was performed for 10 min to remove the ligands introduced during the synthesis process and prevent their interference in the photocatalytic N<sub>2</sub> fixation experiment.

**2.1.3. Preparation of BiVO<sub>4</sub>/V<sub>S</sub>-MoS<sub>2</sub>.** V<sub>S</sub>-MoS<sub>2</sub> nanosheets (30 mg) and BiVO<sub>4</sub> nanocrystals (10 mg) were dispersed in toluene (10 mL). The mixture was ultrasonicated for 10 min and stirred for 3 h in the dark. The suspension was centrifuged followed by washing 3 times with hexane. The BiVO<sub>4</sub>/V<sub>S</sub>-MoS<sub>2</sub> heterojunction can be obtained after vacuum drying at 60 °C for 12 h. In addition, a series of samples can be obtained by adjusting the mass ratio of BiVO<sub>4</sub> and V<sub>S</sub>-MoS<sub>2</sub> as 10 mg : 10 mg, 10 mg : 20 mg, 10 mg : 40 mg, denoted as BiVO<sub>4</sub>/V<sub>S</sub>-MoS<sub>2</sub> (1/1), BiVO<sub>4</sub>/V<sub>S</sub>-MoS<sub>2</sub> (1/2) and BiVO<sub>4</sub>/V<sub>S</sub>-MoS<sub>2</sub> (1/4), respectively.

### 2.2. Photocatalytic N<sub>2</sub> reduction experiment

The photocatalytic N<sub>2</sub> reduction reactions were carried out in a gas–solid reaction system (25 °C). 20 mg of photocatalyst was placed on the sample table of the reactor. 200 μL of water was injected into the bottom of the reactor as the proton source. Before initiating the photocatalytic reactions, the system was heated to produce water vapor. The system was meticulously degassed to remove air with N<sub>2</sub> (99.999%), where N<sub>2</sub> was bubbled through 1 M HCl as well as a mixed solution of potassium permanganate and KOH to ensure the removal of potential contaminants. A 300 W xenon lamp equipped with a UVVISCUT400 filter was employed as the light source (light intensity of 100 mW cm<sup>-2</sup>). For detection, 2 mL of H<sub>2</sub>O was injected into the system to dissolve the product to form the product solution.

### 2.3. Product detection

**2.3.1. Detection of NH<sub>4</sub><sup>+</sup>.** The NH<sub>4</sub><sup>+</sup> concentration was determined with the indophenol blue method as follows: three chromogenic solutions were first prepared, divided into chromogenic agent A, chromogenic agent B, and chromogenic agent C. Chromogenic agent A was prepared by mixing NaOH (4 g), salicylic acid (5 g), and sodium citrate (5 g); chromogenic agent B was obtained by preparing a 0.05 M NaClO aqueous solution; chromogenic agent C was prepared by using 0.1 g sodium nitroferricyanide solution. The product solution (2 mL) was mixed with reagent A (2 mL), reagent B (1 mL), and reagent C (200 μL), and then left for two hours to be detected. Finally, the absorbance at a wavelength of 655 nm was measured to quantify the NH<sub>4</sub><sup>+</sup> content according to the established standard curve of the NH<sub>4</sub>Cl solution.

**2.3.2. Detection of NO<sub>3</sub><sup>-</sup>.** The specific process is as follows: first, prepare 1.0 ppm, 0.5 ppm, 0.2 ppm, and 0.1 ppm solutions of NaNO<sub>3</sub> as the standard solutions to establish the standard curve. Then, the reaction solution (2 mL) was detected by using a model NEXION300 ion chromatograph.

**2.3.3. Detection of NO<sub>2</sub><sup>-</sup>.** The colorimetric method for the detection of NO<sub>2</sub><sup>-</sup> concentration is as follows: color reagent A was prepared by dissolving sulfonamide (0.5 g) in 50 mL of HCl solution (2 M); color reagent B was prepared by dissolving *N*-(1-naphthyl) ethylenediamine hydrochloride (20 mg) in 20 mL of



ultrapure water. The reaction solution (2 mL) was mixed with color reagent A (40  $\mu$ L) and color reagent B (40  $\mu$ L), and then left in the dark for 10 min. The absorbance was characterized by UV-vis absorption spectroscopy, and the content of  $\text{NO}_2^-$  was quantified according to the established standard curve at a wavelength of 540 nm.

**2.3.4. Detection of  $\text{N}_2\text{H}_4$ .** The Watt–Chrisp method was employed to determine the concentration of hydrazine hydrate as follows: the color reagent was prepared by mixing *N,N*-dimethyl-4-aminobenzaldehyde (2 g), concentrated HCl (10 mL), and ethanol (100 mL). The reaction solution (2 mL) was mixed with the color reagent (2 mL), and then left in the dark for 15 min. The absorbance at  $\sim 458$  nm was obtained, and the content of  $\text{N}_2\text{H}_4$  was quantified according to the established standard curve.

#### 2.4. *In situ* diffuse reflectance infrared Fourier transform spectra (DRIFTS)

*In situ* diffuse reflectance infrared Fourier transform spectra were recorded using a Bruker IFS 66v Fourier transform spectrometer. The samples were mixed with KBr in a quartz mortar and then placed in an infrared reaction chamber. Pure  $\text{N}_2$  (99.999%) containing water vapor was continuously introduced into the experimental chamber during *in situ* characterization. The IR spectrum of pure KBr was first collected as a background spectrum. The final spectra were obtained by subtracting the background spectrum from the spectrum of the sample.

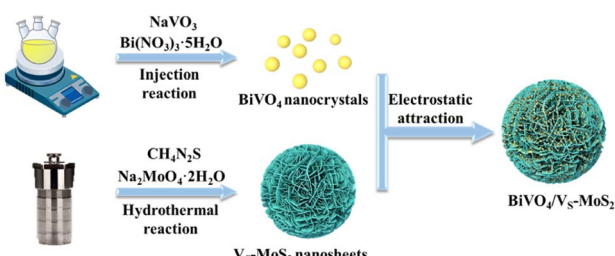
### 3. Results and discussion

#### 3.1. Preparation and structure of $\text{BiVO}_4/\text{V}_\text{S}-\text{MoS}_2$

The synthetic process of  $\text{BiVO}_4/\text{V}_\text{S}-\text{MoS}_2$  is illustrated in Scheme 1. Briefly,  $\text{V}_\text{S}-\text{MoS}_2$  and  $\text{BiVO}_4$  were initially prepared through the hydrothermal method and thermal injection method, respectively. The measured zeta potential ( $\zeta$ ) of  $\text{V}_\text{S}-\text{MoS}_2$  is negative ( $-45$  mV), opposed with that of  $\text{BiVO}_4$  (33 mV) in toluene (Fig. S1†). This opposite surface charging characteristic of  $\text{V}_\text{S}-\text{MoS}_2$  and  $\text{BiVO}_4$  should facilitate the spontaneous assembly to form  $\text{BiVO}_4/\text{V}_\text{S}-\text{MoS}_2$  in solution. X-ray diffraction (XRD) patterns (Fig. 1a) show that the as-prepared  $\text{V}_\text{S}-\text{MoS}_2$  and  $\text{BiVO}_4$  can be indexed to the  $P63/mmc(194)$  hexagonal space group (PDF card no. 01-075-1539) and  $I2/a(15)$  monoclinic space group (PDF card no. 00-014-0688),

respectively. The characteristic diffraction peaks at  $14.39^\circ$ ,  $32.8^\circ$ ,  $39.65^\circ$  and  $58.56^\circ$  of  $\text{V}_\text{S}-\text{MoS}_2$  correspond to the (002), (100), (103), and (110) crystal planes. The diffraction peaks of  $\text{BiVO}_4$  are located at  $18.67^\circ$ ,  $28.95^\circ$ ,  $35.22^\circ$ ,  $39.78^\circ$ ,  $46.71^\circ$ ,  $49.96^\circ$ , and  $59.26^\circ$ , corresponding to the (110), (121), (002), (211), (240), (−202), and (123) crystal planes. Notably, the diffraction pattern of  $\text{BiVO}_4/\text{V}_\text{S}-\text{MoS}_2$  contains the characteristic peaks of both  $\text{V}_\text{S}-\text{MoS}_2$  and  $\text{BiVO}_4$ , indicating the successful loading of  $\text{BiVO}_4$  nanocrystals onto  $\text{V}_\text{S}-\text{MoS}_2$  nanosheets. Scanning electron microscopy (SEM) and transmission electron microscopy (TEM) measurements revealed that  $\text{V}_\text{S}-\text{MoS}_2$  exhibits a nanoflower morphology (Fig. 1b), which is formed by the gathering of nanosheets (Fig. 1c). Atomic force microscopy (AFM) analysis in Fig. S2† further confirmed that  $\text{V}_\text{S}-\text{MoS}_2$  has a nanosheet morphology with a mean thickness of  $\sim 3$  nm. TEM images of pure  $\text{BiVO}_4$  and  $\text{BiVO}_4/\text{V}_\text{S}-\text{MoS}_2$  (Fig. 1d and e) show that  $\text{BiVO}_4$  nanocrystals are interspersed on  $\text{V}_\text{S}-\text{MoS}_2$  nanosheets, with an average size of  $\sim 5$  nm, which is almost identical to that of the pure  $\text{BiVO}_4$  nanocrystal (Fig. S3†). Further high-resolution TEM (HRTEM) analysis (Fig. 1f) showed clear lattice fringes of  $2.72$  Å and  $3.08$  Å, corresponding to the (100) plane of  $\text{V}_\text{S}-\text{MoS}_2$  (ref. 35) and the (121) plane of monoclinic  $\text{BiVO}_4$  (ref. 36) (Fig. S4†), respectively, confirming the presence of  $\text{BiVO}_4$  nanocrystals on the surface of  $\text{V}_\text{S}-\text{MoS}_2$  nanosheets. The corresponding energy-dispersive X-ray spectroscopy (EDS) mapping analysis (Fig. 1g) demonstrated the homogeneous distribution of Mo, S, Bi, V, and O elements on  $\text{BiVO}_4/\text{V}_\text{S}-\text{MoS}_2$ , further verifying the construction of  $\text{BiVO}_4/\text{V}_\text{S}-\text{MoS}_2$ .

To gain insights into the structural characteristics of the as-prepared photocatalysts, electron paramagnetic resonance (EPR) measurements were performed initially. As depicted in Fig. 1h, a distinct EPR signal at  $g = 2.003$  can be recognized for  $\text{V}_\text{S}-\text{MoS}_2$ , signifying the formation of the sulfur vacancies on the surface of  $\text{V}_\text{S}-\text{MoS}_2$ .<sup>37</sup> In the case of  $\text{BiVO}_4/\text{V}_\text{S}-\text{MoS}_2$ , a stronger EPR signal is detected, providing evidence for the formation of heterojunction interfaces, which can turn spin-coupled electron pairs into unpaired electron states.<sup>38</sup> Sulfur vacancies can serve as active sites to promote carrier capture and  $\text{N}_2$  adsorption and activation.<sup>39</sup> The X-ray photoelectron spectra (XPS) were further analyzed to investigate the potential interfacial interaction and charge transfer processes within the  $\text{BiVO}_4/\text{V}_\text{S}-\text{MoS}_2$  heterojunction. Doublet XPS characteristic peaks can be identified at  $229.3$  eV and  $232.4$  eV in pure  $\text{V}_\text{S}-\text{MoS}_2$ , attributed to Mo  $3d_{5/2}$  and Mo  $3d_{3/2}$  (Fig. S5a†), which can confirm the reduction of  $\text{Mo}^{6+}$  to  $\text{Mo}^{4+}$  during the growth of  $\text{V}_\text{S}-\text{MoS}_2$  nanosheets.<sup>40</sup> In addition, a comparison between pure  $\text{V}_\text{S}-\text{MoS}_2$ ,  $\text{BiVO}_4$ , and  $\text{BiVO}_4/\text{V}_\text{S}-\text{MoS}_2$  reveals noticeable shifts in binding energy for Mo 3d, S 2p, Bi 4f, and V 2p. Specifically, Mo 3d and S 2p exhibit positive shifts of  $0.50$  eV and  $0.20$  eV, while Bi 4f and V 2p display negative shifts of  $0.20$  eV and  $0.20$  eV, respectively (Fig. S5b–d†). These charge redistributions within the  $\text{BiVO}_4/\text{V}_\text{S}-\text{MoS}_2$  heterojunction reflect a strong chemical interaction at the interface of the  $\text{BiVO}_4/\text{V}_\text{S}-\text{MoS}_2$  heterojunction. This robust interfacial electronic coupling in  $\text{BiVO}_4/\text{V}_\text{S}-\text{MoS}_2$  is expected to facilitate the charge transfer between the  $\text{V}_\text{S}-\text{MoS}_2$  nanosheets and  $\text{BiVO}_4$  nanocrystals.



**Scheme 1** Schematic illustration of the preparation process of  $\text{BiVO}_4/\text{V}_\text{S}-\text{MoS}_2$ .



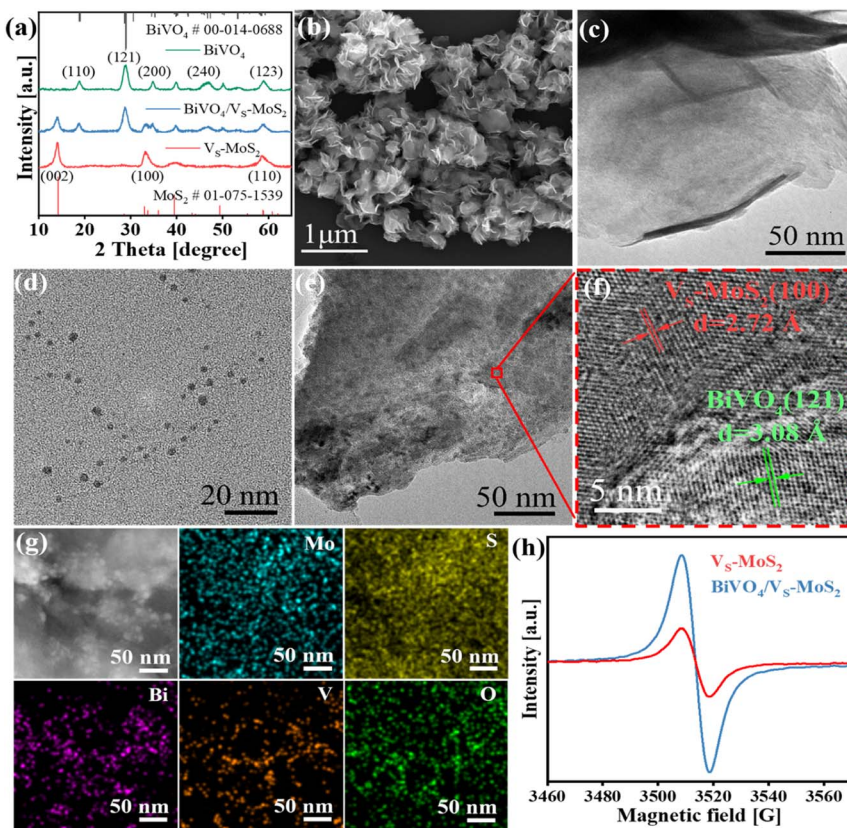


**Fig. 1** (a) XRD patterns of  $V_s$ -MoS<sub>2</sub>, BiVO<sub>4</sub>, and BiVO<sub>4</sub>/V<sub>s</sub>-MoS<sub>2</sub>. (b and c) SEM and TEM images of a V<sub>s</sub>-MoS<sub>2</sub> nanosheet. (d) TEM image of a BiVO<sub>4</sub> nanocrystal. (e–g) TEM, HRTEM, and corresponding EDS images of BiVO<sub>4</sub>/V<sub>s</sub>-MoS<sub>2</sub>. (h) EPR spectra of V<sub>s</sub>-MoS<sub>2</sub> and BiVO<sub>4</sub>/V<sub>s</sub>-MoS<sub>2</sub>.

### 3.2. S-scheme mechanism of the BiVO<sub>4</sub>/V<sub>s</sub>-MoS<sub>2</sub> heterojunction

The energy levels and interfacial charge transfer processes of BiVO<sub>4</sub>/V<sub>s</sub>-MoS<sub>2</sub> were explored to evaluate the photocatalytic N<sub>2</sub> reduction potential of the as-prepared photocatalysts. Fig. 2a and b show the UV-vis diffuse reflectance spectra (DRS), revealing a good light response for both the V<sub>s</sub>-MoS<sub>2</sub> nanosheets and BiVO<sub>4</sub> nanocrystals. From the corresponding Tauc plots (insets of Fig. 2a and b), the band gaps ( $E_g$ ) of V<sub>s</sub>-MoS<sub>2</sub> and BiVO<sub>4</sub> can be deduced to be 1.71 eV and 2.22 eV, respectively. To ascertain the energy band structures of V<sub>s</sub>-MoS<sub>2</sub> and BiVO<sub>4</sub>, the onset edge ( $E_i$ ) and the secondary electron cutoff ( $E_{cutoff}$ ) were determined by carrying out ultraviolet photoelectron spectroscopy (UPS) (Fig. 2c). According to the equation  $E_{VB} = 21.22 - (E_{cutoff} - E_i)$ , the valence band edge potentials ( $E_{VB}$ ) can be calculated to be 1.35 V and 2.23 V *versus* the standard hydrogen electrode (*vs.* NHE) for V<sub>s</sub>-MoS<sub>2</sub> and BiVO<sub>4</sub>, respectively. By combining the values from  $E_g$  and  $E_{VB}$  analysis, the corresponding conduction band edge potentials ( $E_{CB}$ ) can be calculated to be -0.36 V and 0.01 V (*vs.* NHE) for V<sub>s</sub>-MoS<sub>2</sub> and BiVO<sub>4</sub>, respectively. The resultant energy band structures of V<sub>s</sub>-MoS<sub>2</sub> and BiVO<sub>4</sub> are presented in Fig. 2d. The photogenerated electrons in V<sub>s</sub>-MoS<sub>2</sub> possess sufficient energy to drive the photoreduction of N<sub>2</sub> to NH<sub>3</sub> (-0.13 V *vs.* NHE),<sup>41</sup> while their driving force for H<sub>2</sub>O oxidation is relatively weak. Meanwhile, the photogenerated holes in BiVO<sub>4</sub> can trigger H<sub>2</sub>O photooxidation

to O<sub>2</sub> (0.82 V *vs.* NHE, pH = 7), while they are insufficient for the photoreduction of N<sub>2</sub>. In addition, the Fermi levels were also estimated according to the UPS spectra, to be -4.62 eV and -5.27 eV (*vs.* vacuum) for V<sub>s</sub>-MoS<sub>2</sub> and BiVO<sub>4</sub>, respectively. These results reveal that both V<sub>s</sub>-MoS<sub>2</sub> and BiVO<sub>4</sub> are n-type semiconductors, consistent with the results from the Mott-Schottky tests, where the slopes of Mott-Schottky curves for both BiVO<sub>4</sub> and V<sub>s</sub>-MoS<sub>2</sub> are positive (Fig. S6†). From the above results and analysis, we can preliminarily deduce that, given the higher Fermi level of V<sub>s</sub>-MoS<sub>2</sub> compared to that of BiVO<sub>4</sub>, the free electrons in V<sub>s</sub>-MoS<sub>2</sub> would spontaneously flow to BiVO<sub>4</sub> to establish a Fermi level equilibrium upon contact (Fig. S7(I-II)†). A built-in electric field and band bending of the interface in BiVO<sub>4</sub>/V<sub>s</sub>-MoS<sub>2</sub> would be formed. Driven by the interfacial built-in electric field, photogenerated electrons in BiVO<sub>4</sub> would recombine with the photogenerated holes in V<sub>s</sub>-MoS<sub>2</sub> (Fig. S7(III)†), facilitating the formation of the S-scheme charge transfer pathway.

To scrutinize the S-scheme charge transfer pathway in the BiVO<sub>4</sub>/V<sub>s</sub>-MoS<sub>2</sub> heterojunction, *in situ* irradiated XPS (ISI-XPS) spectra were first measured to detect photoinduced changes in the electron cloud density around the nuclei of elements. As depicted in Fig. S8a and b,† the binding energies of Mo 3d and V 2p in BiVO<sub>4</sub>/V<sub>s</sub>-MoS<sub>2</sub> demonstrate a negative displacement (~0.40 eV) and positive movement (~0.30 eV) under illumination, respectively, compared with those in the dark. These



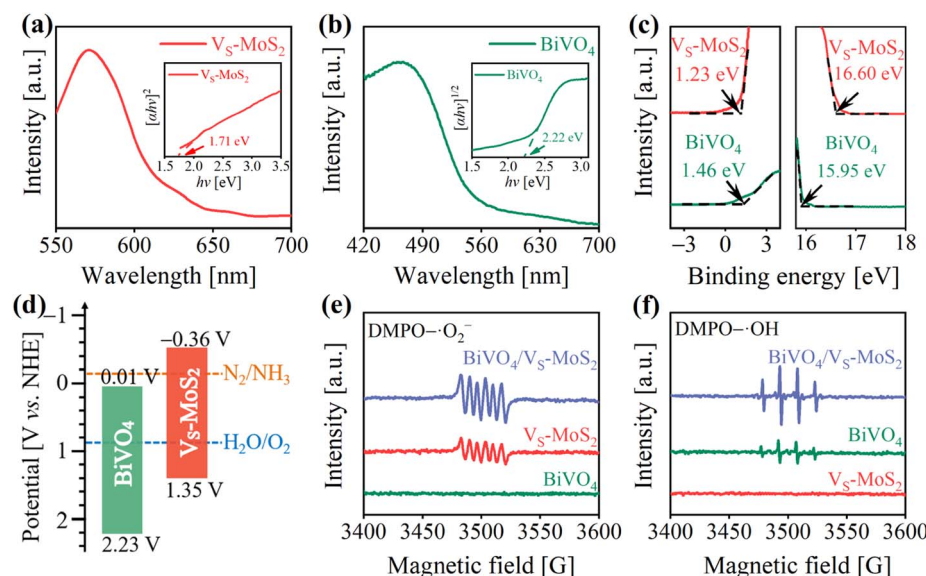


Fig. 2 (a and b) UV-vis DRS spectra of  $V_S\text{-MoS}_2$  and  $\text{BiVO}_4$ . The insets show the corresponding Tauc plots. (c) UPS spectra of  $V_S\text{-MoS}_2$  and  $\text{BiVO}_4$ . (d) Energy band structures of  $V_S\text{-MoS}_2$  and  $\text{BiVO}_4$  (pH = 7). EPR signals of (e) DMPO- $\cdot\text{O}_2^-$  and (f) DMPO- $\cdot\text{OH}$  over  $V_S\text{-MoS}_2$ ,  $\text{BiVO}_4/V_S\text{-MoS}_2$  under illumination.

binding energy changes indicate the accumulation of photo-generated electrons on  $V_S\text{-MoS}_2$  and photogenerated holes on  $\text{BiVO}_4$ , revealing the occurrence of S-scheme interfacial charge transfer within the  $\text{BiVO}_4/V_S\text{-MoS}_2$  heterojunction. To further confirm this S-scheme interfacial charge transfer mechanism in the  $\text{BiVO}_4/V_S\text{-MoS}_2$  heterojunction, the EPR spectra were recorded using 5,5-dimethyl-1-pyrroline N-oxide (DMPO) as the trapping agent.<sup>42</sup> In the case of pure  $V_S\text{-MoS}_2$ , only the DMPO- $\cdot\text{O}_2^-$  characteristic signal can be identified (Fig. 2e), as its  $E_{\text{VB}}$  potential is insufficient to drive the oxidation of  $\text{H}_2\text{O}$  to  $\cdot\text{OH}$ . Conversely, in pure  $\text{BiVO}_4$ , only the DMPO- $\cdot\text{OH}$  characteristic signal can be recognized (Fig. 2f), due to the insufficient driving force of photogenerated electrons in  $E_{\text{CB}}$  to trigger the reduction of  $\text{O}_2$  to  $\cdot\text{O}_2^-$  ( $-0.33$  V vs. NHE). For the  $\text{BiVO}_4/V_S\text{-MoS}_2$  heterojunction, more obvious DMPO- $\cdot\text{O}_2^-$  and DMPO- $\cdot\text{OH}$  signals can be simultaneously identified, providing compelling evidence for the establishment of an interfacial S-scheme charge transport channel. That is to say, the photogenerated electrons in  $\text{BiVO}_4$  and the photogenerated holes in  $V_S\text{-MoS}_2$  initially recombine through the interfacial S-scheme channel, leading to the accumulation of photogenerated holes on  $\text{BiVO}_4$  and photogenerated electrons on  $V_S\text{-MoS}_2$ . This spatial separation of charge carriers in the  $\text{BiVO}_4/V_S\text{-MoS}_2$  heterojunction would more effectively promote their participation in the redox reaction.

### 3.3. Photogenerated carrier evolution

In general, the evolution of photogenerated charges within photocatalysts plays a pivotal role in determining their photocatalytic activity.<sup>43,44</sup> To evaluate the behavior of photogenerated carriers in  $\text{BiVO}_4/V_S\text{-MoS}_2$ , steady-state photoluminescence (PL) spectrum measurements were first performed. As presented in Fig. 3a, the PL spectrum of  $\text{BiVO}_4$  displays an intrinsic emission

band at  $\sim 490$  nm under 365 nm excitation, which is related to photogenerated electron-hole recombination. Upon the construction of the  $\text{BiVO}_4/V_S\text{-MoS}_2$  heterojunction, the PL spectrum exhibits significant quenching, indicating the effective transfer of photogenerated carriers between the  $\text{BiVO}_4$  nanocrystals and  $V_S\text{-MoS}_2$  nanosheets. In addition, the photoelectrochemical properties of the samples were characterized to assess the potential positive influence of the construction of a heterostructure on charge evolution behavior. Notably, under light irradiation,  $\text{BiVO}_4/V_S\text{-MoS}_2$  exhibits a smaller charge-transport resistance compared with both pure  $\text{BiVO}_4$  and  $V_S\text{-MoS}_2$  (Fig. 3b and Table S1†), indicating that the construction of the electric field in the heterojunction improves the charge transport characteristics. From the transient photocurrent ( $I-t$ ) measurements (Fig. 3c), it is evident that  $\text{BiVO}_4/V_S\text{-MoS}_2$  has a higher current density than both  $\text{BiVO}_4$  and  $V_S\text{-MoS}_2$ , providing further evidence of expedited charge separation kinetics within the  $\text{BiVO}_4/V_S\text{-MoS}_2$  heterojunction. Moreover, to more intuitively reveal the space charge separation, Kelvin probe force microscopy (KPFM) was utilized to measure the surface photovoltage (SPV) response of photocatalysts under light. Atomic force microscope (AFM) images (Fig. 3d and f) present the morphology outline of  $V_S\text{-MoS}_2$  and  $\text{BiVO}_4/V_S\text{-MoS}_2$  nanosheet clusters, which are basically consistent with the SEM results (Fig. 1b). Under illumination, the SPV response zone (Fig. 3e and g) emerges, aligning with the morphology outlines of the samples. These observations also indicate the spatial charge separation and redistribution after light irradiation.<sup>45</sup> As shown in Fig. 3h, pure  $V_S\text{-MoS}_2$  presents a feeble SPV signal under light irradiation, primarily due to rapid photogenerated carrier recombination. Benefiting from the construction of heterojunctions,  $\text{BiVO}_4/V_S\text{-MoS}_2$  displays a noticeable enhancement of the SPV response, of  $\sim 100$  mV, far surpassing



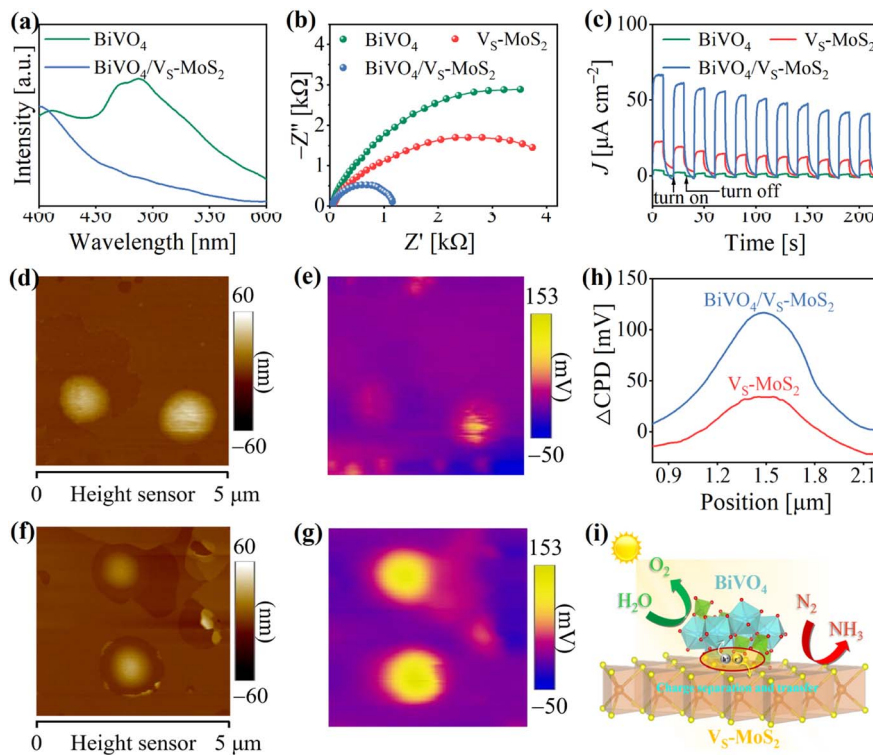


Fig. 3 (a) Steady-state photoluminescence spectra of  $\text{BiVO}_4$  and  $\text{BiVO}_4/\text{Vs-MoS}_2$ . (b and c) EIS plots and  $I-t$  curves of  $\text{BiVO}_4$ ,  $\text{Vs-MoS}_2$ , and  $\text{BiVO}_4/\text{Vs-MoS}_2$  plotted at a bias potential of  $-0.4$  V vs.  $\text{Ag}/\text{AgCl}$ . AFM height images of (d)  $\text{Vs-MoS}_2$  and (f)  $\text{BiVO}_4/\text{Vs-MoS}_2$ . SPV images of (e)  $\text{Vs-MoS}_2$  and (g)  $\text{BiVO}_4/\text{Vs-MoS}_2$  under illumination. (h) Potential difference changes ( $\Delta\text{CPD}$ ) of  $\text{Vs-MoS}_2$  and  $\text{BiVO}_4/\text{Vs-MoS}_2$  by subtracting the potential under dark conditions from that under illumination. (i) Schematic illustration of the photogenerated carrier separation.

that of pure  $\text{Vs-MoS}_2$ . Ultimately, these characterization studies underscore that the construction of heterojunctions can promote charge separation, and enhance the accumulation of electrons/holes on  $\text{Vs-MoS}_2$  and  $\text{BiVO}_4$ , respectively, which is beneficial for these carriers to participate in the subsequent multi-electron transfer processes during the photoreduction  $\text{N}_2$  reaction (Fig. 3i).

### 3.4. Photocatalytic $\text{N}_2$ reduction activity

The photocatalytic  $\text{N}_2$  reduction reactions were conducted in a gas–solid reaction apparatus (Fig. S9†) containing  $\text{N}_2$  and  $\text{H}_2\text{O}$  vapor under simulated sunlight irradiation ( $100 \text{ mW cm}^{-2}$ ). To ensure the accuracy of our experiments, the samples were pre-treated with a DMSO solution of KI. This step is crucial to remove any residual ligands introduced during the synthesis process, preventing any interference with the experimental results (Fig. S10,† details are described in the Experimental section). The photocatalytic activities were evaluated by evaluating the  $\text{NH}_4^+$  production using the indophenol blue method (Fig. S11,† details are described in the Experimental section).<sup>46</sup> As illustrated in Fig. S12,† a prominent absorption signal at  $\sim 655$  nm can be observed, indicating that  $\text{N}_2$  is effectively photoreduced to  $\text{NH}_3$  in the presence of light for  $\text{BiVO}_4/\text{Vs-MoS}_2$ . The  $\text{NH}_3$  generation performances for the as-prepared photocatalysts are presented in Fig. 4a and S13.† For pure  $\text{BiVO}_4$ , there is virtually no  $\text{NH}_3$  synthesis activity due to the

insufficient driving force of electron energy in its conduction band (Fig. 2d). Meanwhile,  $\text{Vs-MoS}_2$  exhibits a weak  $\text{N}_2$  photo-reduction to  $\text{NH}_3$  activity, with a rate of  $20.0 \pm 1.1 \text{ } \mu\text{mol g}^{-1} \text{ h}^{-1}$ , resulting from its insufficient thermodynamic driving force for  $\text{H}_2\text{O}$  oxidation and serious charge recombination. Upon combining the  $\text{Vs-MoS}_2$  nanosheets with the  $\text{BiVO}_4$  nanocrystals, the corresponding photocatalytic  $\text{N}_2$  reduction activity improves significantly, reaching  $132.8 \pm 4.2 \text{ } \mu\text{mol g}^{-1} \text{ h}^{-1}$  within 4 hours, which is nearly 7-fold that of pure  $\text{Vs-MoS}_2$ . The apparent quantum efficiency at  $575$  nm can reach  $0.3\%$  (Fig. S14†). Certainly, we also analyzed the  $\text{NH}_4^+$  production by ion chromatography (Fig. S15†), and the results are in agreement with those obtained by the indophenol blue method. Obviously, this improvement of  $\text{NH}_3$  evolution activity can be attributed to the increased driving force for water oxidation and the enhanced separation of photogenerated carriers in the  $\text{BiVO}_4/\text{Vs-MoS}_2$  heterojunction, compared with pure  $\text{Vs-MoS}_2$  nanosheets. By adjusting the mass ratio of  $\text{BiVO}_4$  and  $\text{Vs-MoS}_2$  (Fig. S16†), the  $\text{NH}_3$  evolution activities of the samples were screened, in which  $\text{BiVO}_4/\text{Vs-MoS}_2$  with a mass ratio ( $\text{BiVO}_4 : \text{Vs-MoS}_2$ ) of  $1 : 3$  exhibits the best performance (Fig. 4a).

Moreover, the  $\text{O}_2$  evolution activity of  $\text{BiVO}_4/\text{Vs-MoS}_2$  was also measured through a gas chromatograph, to be  $110.0 \pm 4.5 \text{ } \mu\text{mol g}^{-1} \text{ h}^{-1}$  (Fig. S17†). This result suggests that the rate of consumed electrons ( $R_{\text{electron}}$ ) for  $\text{N}_2$  reduction to  $\text{NH}_3$  is nearly equal to the rate of consumed holes ( $R_{\text{hole}}$ ) for water oxidation to  $\text{O}_2$ , in accordance with the formulae of  $R_{\text{electron}} = 3 \times R_{\text{NH}_3}$  and



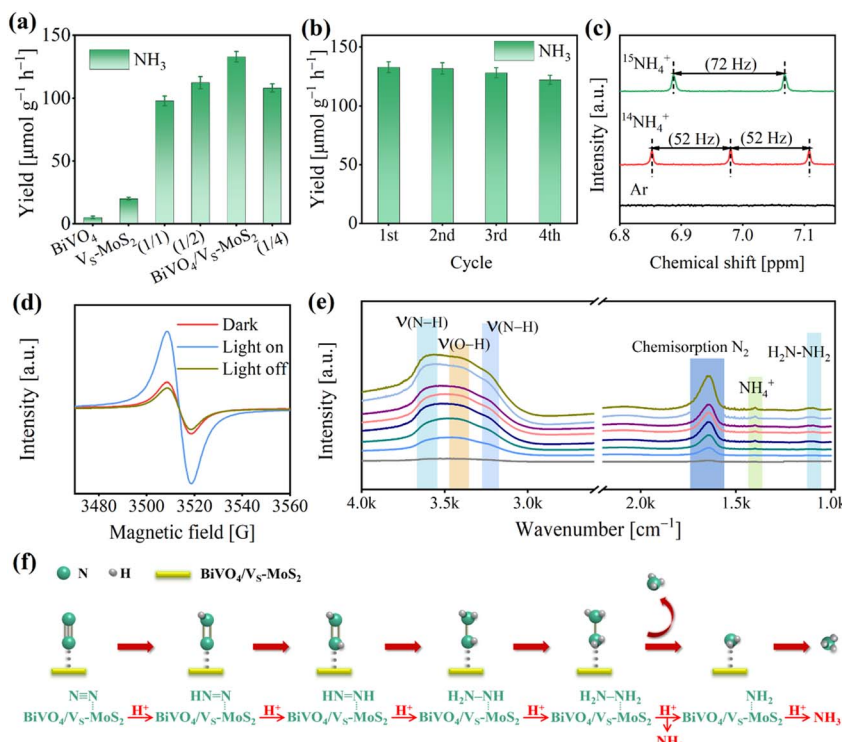


**Fig. 4** (a) Photocatalytic NH<sub>3</sub> production rates for BiVO<sub>4</sub>, V<sub>S</sub>-MoS<sub>2</sub>, BiVO<sub>4</sub>/V<sub>S</sub>-MoS<sub>2</sub>, BiVO<sub>4</sub>/V<sub>S</sub>-MoS<sub>2</sub> (1/1), BiVO<sub>4</sub>/V<sub>S</sub>-MoS<sub>2</sub> (1/2), and BiVO<sub>4</sub>/V<sub>S</sub>-MoS<sub>2</sub> (1/4) under 4 h light irradiation. (b) NH<sub>3</sub> synthesis for four cyclic tests of BiVO<sub>4</sub>/V<sub>S</sub>-MoS<sub>2</sub>. (c) The <sup>1</sup>H NMR spectra of products with <sup>14</sup>N<sub>2</sub> or <sup>15</sup>N<sub>2</sub> as the reaction atmosphere. (d) *In situ* EPR spectra of BiVO<sub>4</sub>/V<sub>S</sub>-MoS<sub>2</sub> in the dark or under light irradiation in a N<sub>2</sub> atmosphere or light off in a N<sub>2</sub> atmosphere. (e) *In situ* DRIFTS spectra of the photoreduction N<sub>2</sub> reaction. (f) The proposed reaction pathway of the photoreduction N<sub>2</sub> reaction.

$R_{\text{hole}} = 4 \times R_{\text{O}_2}$ . This balance signifies the effective utilization of the photogenerated electrons and holes. Based on the above analysis, the whole photocatalytic reaction including N<sub>2</sub> reduction and H<sub>2</sub>O oxidation by BiVO<sub>4</sub>/V<sub>S</sub>-MoS<sub>2</sub> can be described as  $2\text{N}_2 + 6\text{H}_2\text{O} \rightarrow 4\text{NH}_3 + 3\text{O}_2$ . Additionally, the robustness of BiVO<sub>4</sub>/V<sub>S</sub>-MoS<sub>2</sub> was evaluated by reemploying the photocatalyst in four cycles of tests (Fig. 4b), which reveals little decrement in activity. In addition, the XRD patterns (Fig. S18<sup>†</sup>) and TEM images (Fig. S19<sup>†</sup>) of BiVO<sub>4</sub>/V<sub>S</sub>-MoS<sub>2</sub> after the photocatalytic reaction exhibit no obvious changes, confirming the good stability of the photocatalyst in this gas-solid photocatalytic system. The Mo 3d and Bi 4f XPS spectra of BiVO<sub>4</sub>/V<sub>S</sub>-MoS<sub>2</sub> after catalysis show almost no significant changes, further suggesting the maintenance of the local coordination environment of the Bi and Mo sites.

To elucidate the origin of NH<sub>3</sub> and O<sub>2</sub> during the photocatalytic reaction, several controlled experiments were carried out using BiVO<sub>4</sub>/V<sub>S</sub>-MoS<sub>2</sub> as the photocatalyst (Fig. S21<sup>†</sup>). In the absence of a photocatalyst (BiVO<sub>4</sub>/V<sub>S</sub>-MoS<sub>2</sub>), N<sub>2</sub>, light, or H<sub>2</sub>O, there is nearly no NH<sub>3</sub> evolution, unequivocally demonstrating that the N<sub>2</sub> reduction reaction is indeed a photocatalytic reaction using BiVO<sub>4</sub>/V<sub>S</sub>-MoS<sub>2</sub> as the photocatalyst with H<sub>2</sub>O as the proton source. According to the characterization by the colorimetric method and ion chromatography (the details are described in the Experimental section), nearly no NO<sub>2</sub><sup>-</sup> and NO<sub>3</sub><sup>-</sup> signals in the product system can be detected before and

after the photocatalytic reaction (Fig. S22 and S23<sup>†</sup>). In addition, we have further measured the N content in the obtained photocatalyst by EDS analysis (Fig. S24 and Table S2<sup>†</sup>), and no N atoms are present. These results confirm that NH<sub>3</sub> remained unoxidized, and substantiate that NH<sub>3</sub> originated solely from N<sub>2</sub> reduction, excluding impurity conversion as a source. To further verify the origin of NH<sub>3</sub> in the product system, isotope labeling experiments were performed using BiVO<sub>4</sub>/V<sub>S</sub>-MoS<sub>2</sub> as the photocatalyst in atmospheres containing <sup>15</sup>N<sub>2</sub>, <sup>14</sup>N<sub>2</sub>, or Ar, respectively (Fig. S25<sup>†</sup>). More specifically, no NH<sub>4</sub><sup>+</sup> signal is detected under a Ar atmosphere in the nuclear magnetic resonance (NMR) spectra, while distinct signals belonging to <sup>15</sup>NH<sub>4</sub><sup>+</sup> or <sup>14</sup>NH<sub>4</sub><sup>+</sup> can be observed in a <sup>15</sup>N<sub>2</sub> or <sup>14</sup>N<sub>2</sub> atmosphere, respectively (Fig. 4c). These results directly confirm that NH<sub>4</sub><sup>+</sup> is indeed generated from the N<sub>2</sub> in the system. In addition, the mass spectrometry analysis of the product (Fig. S26<sup>†</sup>) was also performed, revealing an <sup>18</sup>O<sub>2</sub> signal at  $m/z = 36$ , which confirms that O<sub>2</sub> is produced from H<sub>2</sub>O oxidation.

To gain insight into the photocatalytic N<sub>2</sub> reduction process of the BiVO<sub>4</sub>/V<sub>S</sub>-MoS<sub>2</sub> heterojunction, we conducted further characterization to explore the active sites and monitor the evolution of intermediates during the photocatalytic reaction, by using *in situ* EPR spectra and *in situ* diffuse reflectance infrared Fourier transform spectra (DRIFTS), respectively. As presented in Fig. 4d, the intensity of the sulfur vacancy signal for BiVO<sub>4</sub>/V<sub>S</sub>-MoS<sub>2</sub> exhibits an increment when exposed to light

irradiation for 15 min, and decreases once the light was turned off for 10 min, suggesting that the sulfur vacancies facilitate the trapping of photogenerated electrons from the conduction band.<sup>47,48</sup> The exposed Mo site at the sulfur vacancy is in a coordination unsaturated state, and can act as the photocatalytic active site bonding with N<sub>2</sub>. The trapped photogenerated electrons at sulfur vacancies can transfer to N<sub>2</sub> molecules to achieve N<sub>2</sub> reduction and transformation. As the photocatalytic N<sub>2</sub> reduction reaction proceeded, a series of absorption signals were detected belonging to intermediates adsorbed on BiVO<sub>4</sub>/V<sub>S</sub>-MoS<sub>2</sub> (Fig. 4e). Specifically, an obvious peak at 1648 cm<sup>-1</sup> belonging to the chemisorbed N<sub>2</sub> (-N≡N) appeared,<sup>49</sup> which can be attributed to the efficient adsorption and activation of N<sub>2</sub> by the Mo sites at the vacancies of the nanosheets.<sup>50</sup> The peak at 3432 cm<sup>-1</sup> is attributed to  $\nu$ (O-H) of H<sub>2</sub>O, which serves as the proton source for N<sub>2</sub> activation. The overlapped signal bands at 3230 cm<sup>-1</sup> and 3555 cm<sup>-1</sup> can be attributed to  $\nu$ (N-H) stretching modes of NH<sub>3</sub>, and the peak at 1403 cm<sup>-1</sup> can be attributed to NH<sub>4</sub><sup>+</sup> adsorption. The enhancement of these characteristic signals implies the progression of N<sub>2</sub> activation and conversion to NH<sub>3</sub> via a multistep proton-coupled electron transfer (PCET) process over BiVO<sub>4</sub>/V<sub>S</sub>-MoS<sub>2</sub>. In addition, a peak at 1102 cm<sup>-1</sup> can be identified, originating from the H<sub>2</sub>N-NH<sub>2</sub> characteristic signal.<sup>51</sup> Given that there is no hydrazine formation in the product (Fig. S27†), we thus speculate that the photocatalytic N<sub>2</sub> fixation process on BiVO<sub>4</sub>/V<sub>S</sub>-MoS<sub>2</sub> follows an associative alternating pathway (Fig. 4f). In this pathway, hydrogenation occurs alternatively on two N atoms, with the final step involving the cleavage of the N-N bond to generate the first NH<sub>3</sub> molecule, followed by the last hydrogenation and another NH<sub>3</sub> desorption.

## 4. Conclusions

In summary, we have successfully prepared an S-scheme heterojunction of BiVO<sub>4</sub>/V<sub>S</sub>-MoS<sub>2</sub> by coupling the N<sub>2</sub>-activated component (V<sub>S</sub>-MoS<sub>2</sub>) and the water-oxidized module (BiVO<sub>4</sub>) to facilitate the process of photocatalytic N<sub>2</sub> reduction. BiVO<sub>4</sub>/V<sub>S</sub>-MoS<sub>2</sub> exhibits efficient NH<sub>3</sub> synthesis activity using H<sub>2</sub>O as a proton source under illumination (100 mW cm<sup>-2</sup>), with an NH<sub>3</sub> yield of 132.8  $\mu\text{mol g}^{-1} \text{h}^{-1}$ , nearly 7 times higher than that of pure V<sub>S</sub>-MoS<sub>2</sub>. Our experimental findings underscore the pivotal roles played by the V<sub>S</sub>-MoS<sub>2</sub> nanosheet with sulfur-rich vacancies in enhancing N<sub>2</sub> adsorption and activation. Furthermore, the construction of the S-scheme heterojunction substantially elevates the driving force for H<sub>2</sub>O oxidation and significantly improves charge separation within the system. Moreover, an alternate association pathway for N<sub>2</sub> photoreduction reaction is proposed according to the *in situ* DRIFTS characterization. This study presents an efficient example for achieving the N<sub>2</sub> conversion process under mild conditions.

## Author contributions

Han-Ying Luo: data curation, formal analysis, validation. Zhao-Lei Liu: data curation, formal analysis, validation. Meng-Ran

Zhang: formal analysis, supervision. Yan-Fei Mu: validation, writing – original draft preparation, funding acquisition. Min Zhang: conceptualization, funding acquisition, supervision, validation, writing – reviewing and editing.

## Conflicts of interest

There are no conflicts of interest to declare.

## Acknowledgements

This work was financially supported by the National Natural Science Foundation of China (U21A20286 and 22305214), the National Key R&D Program of China (2022YFA1502902), the Natural Science Foundation of Tianjin City (17JCJQJC43800), the Jiangsu Funding Program for Excellent Postdoctoral Talent, the 111 Project of China (D17003), and the Tianjin Research Innovation Project for Postgraduate Students (2022SKY178).

## References

- 1 J. W. Erisman, M. A. Sutton, J. Galloway, Z. Klimont and W. Winiwarter, *Nat. Geosci.*, 2008, **1**, 636–639.
- 2 X.-B. Li, Z.-K. Xin, S.-G. Xia, X.-Y. Gao, C.-H. Tung and L.-Z. Wu, *Chem. Soc. Rev.*, 2020, **49**, 9028–9056.
- 3 Y. Yang, S.-Q. Wang, H. Wen, T. Ye, J. Chen, C.-P. Li and M. Du, *Angew. Chem., Int. Ed.*, 2019, **58**, 15362–15366.
- 4 S. L. Foster, S. I. P. Bakovic, R. D. Duda, S. Maheshwari, R. D. Milton, S. D. Minteer, M. J. Janik, J. N. Renner and L. F. Greenlee, *Nat. Catal.*, 2018, **1**, 490–500.
- 5 X. Zheng, Y. Yan, X. Li, Y. Liu and Y. Yao, *J. Hazard. Mater.*, 2023, **446**, 130679.
- 6 S. Wang, Y. Wang, T. C. Zhang, X. Jia and S. Yuan, *Nanoscale*, 2023, **15**, 16219–16226.
- 7 Y. Yu, Y. Li, Y. Fang, L. Wen, B. Tu and Y. Huang, *Appl. Catal., B*, 2024, **340**, 123161.
- 8 Z. Zhao, H. Ren, D. Yang, Y. Han, J. Shi, K. An, Y. Chen, Y. Shi, W. Wang, J. Tan, X. Xin, Y. Zhang and Z. Jiang, *ACS Catal.*, 2021, **11**, 9986–9995.
- 9 S. H. W. Kok, J. Lee, W.-K. Chong, B.-J. Ng, X. Y. Kong, W.-J. Ong, S.-P. Chai and L.-L. Tan, *J. Alloys Compd.*, 2023, **952**, 170015.
- 10 J. Di, C. Chen, Y. Wu, Y. Zhao, C. Zhu, Y. Zhang, C. Wang, H. Chen, J. Xiong, M. Xu, J. Xia, J. Zhou, Y. Weng, L. Song, S. Li, W. Jiang and Z. Liu, *Adv. Mater.*, 2022, **34**, 2204959.
- 11 S. Zhang, Y. Zhao, R. Shi, C. Zhou, G. I. N. Waterhouse, Z. Wang, Y. Weng and T. Zhang, *Angew. Chem., Int. Ed.*, 2021, **60**, 2554–2560.
- 12 S. Wang, X. Hai, X. Ding, K. Chang, Y. Xiang, X. Meng, Z. Yang, H. Chen and J. Ye, *Adv. Mater.*, 2017, **29**, 1701774.
- 13 Z. Lu, H. Wang, Y. Tao, S. Zhu, W. Hao, X. Liu, Y. Min and J. Fan, *Nanoscale*, 2023, **15**, 14847–14857.
- 14 C. J. M. van der Ham, M. T. M. Koper and D. G. H. Hitterscheid, *Chem. Soc. Rev.*, 2014, **43**, 5183–5191.
- 15 Y. Xiong, B. Li, Y. Gu, T. Yan, Z. Ni, S. Li, J.-L. Zuo, J. Ma and Z. Jin, *Nat. Chem.*, 2023, **15**, 286–293.



16 S. Liu, Z. Teng, H. Liu, T. Wang, G. Wang, Q. Xu, X. Zhang, M. Jiang, C. Wang, W. Huang and H. Pang, *Angew. Chem., Int. Ed.*, 2022, **61**, e202207026.

17 Y. Lv, S.-W. Ke, Y. Gu, B. Tian, L. Tang, P. Ran, Y. Zhao, J. Ma, J.-L. Zuo and M. Ding, *Angew. Chem., Int. Ed.*, 2023, **62**, e202305246.

18 G. N. Schrauzer and T. D. Guth, *J. Am. Chem. Soc.*, 1977, **99**, 7189–7193.

19 S. Cao, N. Zhou, F. Gao, H. Chen and F. Jiang, *Appl. Catal., B*, 2017, **218**, 600–610.

20 L. Zhang, S. Hou, T. Wang, S. Liu, X. Gao, C. Wang and G. Wang, *Small*, 2022, **18**, 2202252.

21 S. Hu, Y. Li, F. Li, Z. Fan, H. Ma, W. Li and X. Kang, *ACS Sustainable Chem. Eng.*, 2016, **4**, 2269–2278.

22 Y. Zhao, Y. Zhao, G. I. N. Waterhouse, L. Zheng, X. Cao, F. Teng, L.-Z. Wu, C.-H. Tung, D. O'Hare and T. Zhang, *Adv. Mater.*, 2017, **29**, 1703828.

23 H. Su, L. Chen, Y. Chen, R. Si, Y. Wu, X. Wu, Z. Geng, W. Zhang and J. Zeng, *Angew. Chem., Int. Ed.*, 2020, **59**, 20411–20416.

24 G. Zhan, F. Quan, Y. Yao, S. Zhao, X. Liu, H. Gu, Y. Huang, X. Liu, F. Jia and L. Zhang, *Appl. Catal., B*, 2023, **323**, 122186.

25 Q. Li, Y. Shi, Z. Wang, C. Liu, J. Bi, J. C. Yu and L. Wu, *J. Colloid Interface Sci.*, 2023, **652**, 1568–1577.

26 T. He, Z. Zhao, R. Liu, X. Liu, B. Ni, Y. Wei, Y. Wu, W. Yuan, H. Peng, Z. Jiang and Y. Zhao, *J. Am. Chem. Soc.*, 2023, **145**, 6057–6066.

27 X. Dong, K. Wang, Z. Cui, X. Shi, Z. Wang and F. Dong, *Nano Res.*, 2023, **16**, 6679–6686.

28 Z. Ai, M. Huang, D. Shi, M. Yang, H. Hu, B. Zhang, Y. Shao, J. Shen, Y. Wu and X. Hao, *Appl. Catal., B*, 2022, **315**, 121577.

29 Y. Chen, M. Yu, G. Huang, Q. Chen and J. Bi, *Small*, 2022, **18**, 2205388.

30 C. Cheng, J. Zhang, B. Zhu, G. Liang, L. Zhang and J. Yu, *Angew. Chem., Int. Ed.*, 2023, **62**, e202218688.

31 E. Aslan, M. K. Gonc, M. Z. Yigit, A. Sarilmaz, E. Stathatos, F. Ozel, M. Can and I. H. Patir, *Appl. Catal., B*, 2017, **210**, 320–327.

32 Y. Zhang, J. Di, X. Zhu, M. Ji, C. Chen, Y. Liu, L. Li, T. Wei, H. Li and J. Xia, *Appl. Catal., B*, 2023, **323**, 122148.

33 Y. Wang, S. Wang, J. Gan, J. Shen, Z. Zhang, H. Zheng and X. Wang, *ACS Sustainable Chem. Eng.*, 2023, **11**, 1962–1973.

34 Y. Lu, Y. Yang, X. Fan, Y. Li, D. Zhou, B. Cai, L. Wang, K. Fan and K. Zhang, *Adv. Mater.*, 2022, **34**, 2108178.

35 A. Shan, X. Teng, Y. Zhang, P. Zhang, Y. Xu, C. Liu, H. Li, H. Ye and R. Wang, *Nano Energy*, 2022, **94**, 106913.

36 C. Liu, S. Mao, M. Shi, X. Hong, D. Wang, F. Wang, M. Xia and Q. Chen, *Chem. Eng. J.*, 2022, **449**, 137757.

37 X. Guo, E. Song, W. Zhao, S. Xu, W. Zhao, Y. Lei, Y. Fang, J. Liu and F. Huang, *Nat. Commun.*, 2022, **13**, 5954.

38 P. Xia, X. Pan, S. Jiang, J. Yu, B. He, P. M. Ismail, W. Bai, J. Yang, L. Yang, H. Zhang, M. Cheng, H. Li, Q. Zhang, C. Xiao and Y. Xie, *Adv. Mater.*, 2022, **34**, 2200563.

39 Z. Li, G. Gu, S. Hu, X. Zou and G. Wu, *Chin. J. Catal.*, 2019, **40**, 1178–1186.

40 X. Xu, X. Liu, J. Zhao, D. Wu, Y. Du, T. Yan, N. Zhang, X. Ren and Q. Wei, *J. Colloid Interface Sci.*, 2022, **606**, 1374–1379.

41 C. Zhao, X. Li, L. Yue, X. Ren, S. Yuan, Z. Zeng, X. Hu, Y. Wu and Y. He, *ACS Appl. Nano Mater.*, 2023, **6**, 15709–15720.

42 Y.-F. Mu, C. Zhang, M.-R. Zhang, W. Zhang, M. Zhang and T.-B. Lu, *ACS Appl. Mater. Interfaces*, 2021, **13**, 22314–22322.

43 R. Chen, D. Zhang, Z. Wang, D. Li, L. Zhang, X. Wang, F. Fan and C. Li, *J. Am. Chem. Soc.*, 2023, **145**, 4667–4674.

44 A. Kumar, M. Sharma, S. Sheoran, S. Jaiswal, A. Patra, S. Bhattacharya and V. Krishnan, *Nanoscale*, 2023, **15**, 11667–11680.

45 R. Chen, Z. Ren, Y. Liang, G. Zhang, T. Dittrich, R. Liu, Y. Liu, Y. Zhao, S. Pang, H. An, C. Ni, P. Zhou, K. Han, F. Fan and C. Li, *Nature*, 2022, **610**, 296–301.

46 M.-M. Shi, D. Bao, B.-R. Wulan, Y.-H. Li, Y.-F. Zhang, J.-M. Yan and Q. Jiang, *Adv. Mater.*, 2017, **29**, 1606550.

47 Z. Wang, J. Zhu, X. Zu, Y. Wu, S. Shang, P. Ling, P. Qiao, C. Liu, J. Hu, Y. Pan, J. Zhu, Y. Sun and Y. Xie, *Angew. Chem., Int. Ed.*, 2022, **61**, e202203249.

48 L. Luo, X. Han, K. Wang, Y. Xu, L. Xiong, J. Ma, Z. Guo and J. Tang, *Nat. Commun.*, 2023, **14**, 2690.

49 Y. Zhang, J. Di, X. Qian, M. Ji, Z. Tian, L. Ye, J. Zhao, S. Yin, H. Li and J. Xia, *Appl. Catal., B*, 2021, **299**, 120680.

50 Y. Bo, H. Wang, Y. Lin, T. Yang, R. Ye, Y. Li, C. Hu, P. Du, Y. Hu, Z. Liu, R. Long, C. Gao, B. Ye, L. Song, X. Wu and Y. Xiong, *Angew. Chem., Int. Ed.*, 2021, **60**, 16085–16092.

51 Y. Yao, S. Zhu, H. Wang, H. Li and M. Shao, *J. Am. Chem. Soc.*, 2018, **140**, 1496–1501.

